Electronic Supplementary Information

Covalently Bonded Interfaces with Delocalized π Electrons in MOF-in-MOF Heterojunction for Efficient Gas-Solid Phase CO_2 Photoreduction

Rou-Yu Li, Wenyu Yuan*, Meng-Ru Cui, Boda Li, Hui Zhang, Zhenhao Peng, Quan-Guo Zhai *

Key Laboratory of Macromolecular Science of Shaanxi Province, School of Chemistry & Chemical Engineering, Shaanxi Normal University, Xi'an, Shaanxi, 710062, China.

*Email: wenyu.yuan@snnu.edu.cn, zhaiqg@snnu.edu.cn

This PDF file includes:

Supplementary calculation details

The equation of plotting standard curve according to the relations of chromatographic peak area and concentration of target gases are shown as follows:

$$n=\frac{c*180*1000}{1000000*22.4} \quad \mu \text{ mol} \tag{1}$$

The yield (R), evolution and selectivity of CO and CH_4 for the catalyst were tested under the same reaction conditions as the standard conditions and calculated from Equation (2), Equation (3) and Equation (4).

$$Evolution=\frac{n}{m}\mu mo\lg^{-1} \tag{2}$$

$$R=\frac{Evolution}{t}\mu mo\lg^{-1}h^{-1} \tag{3}$$

$$S_{CO}=\frac{c_{CO}}{c_{CO}+c_{CH_4}} \tag{4}$$

The AQE was calculated according to the following equation where ν (mol s^{-1}) is the reaction rate of evolved CO_2 or CH_4 molecules, K is the number of electrons transferred by the reaction, I is the optical power density, S is the incident light area, λ is the incident wavelength and A is the absorbance of the reaction system.

$$AQE=\frac{1.2\times10^{8}(\nu\times K)}{(I\times S\times\lambda\times A)}\times100\% \tag{5}$$

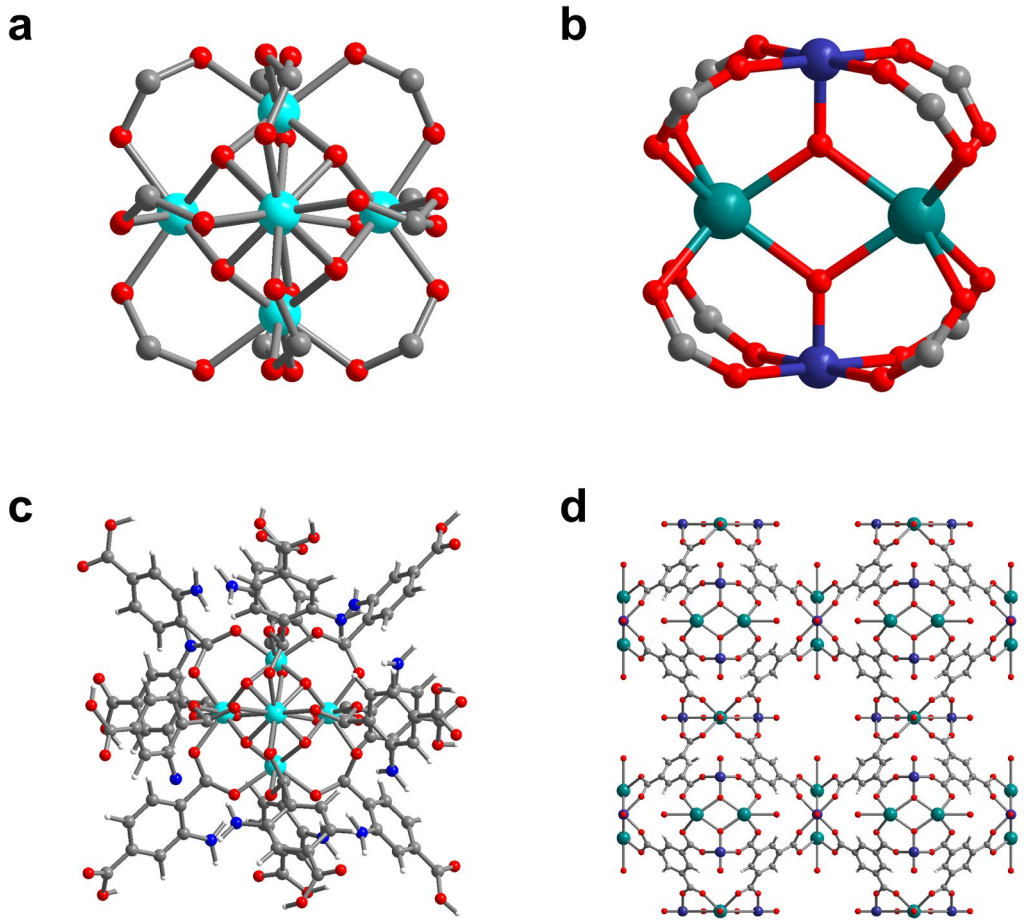

Fig. S1 The 3D metal–organic coordination framework of (a, c) UiO-66-NH_2 and (b, d) MUV-10.

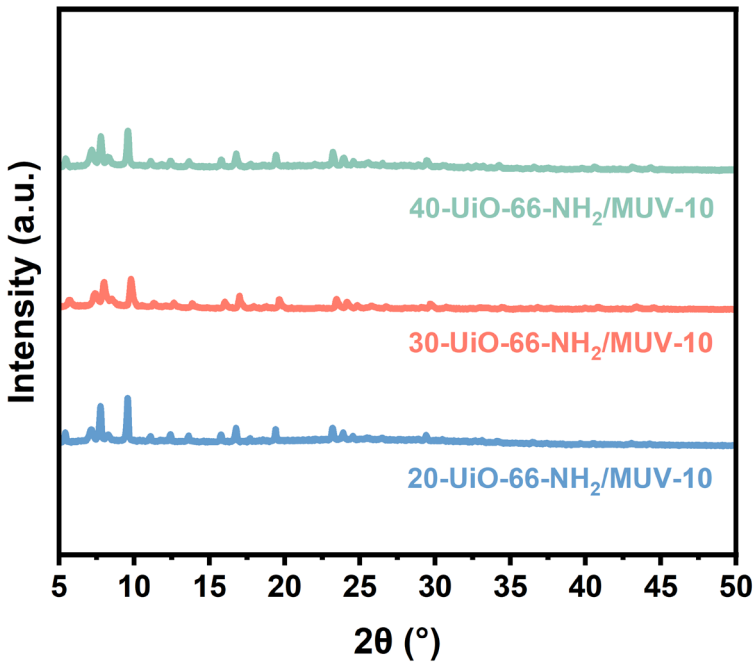

Fig. S2 XRD patterns of 20-UiO-66-NH_2/MUV-10, 30-UiO-66-NH_2/MUV-10, and 30-UiO-66-NH_2/MUV-10.

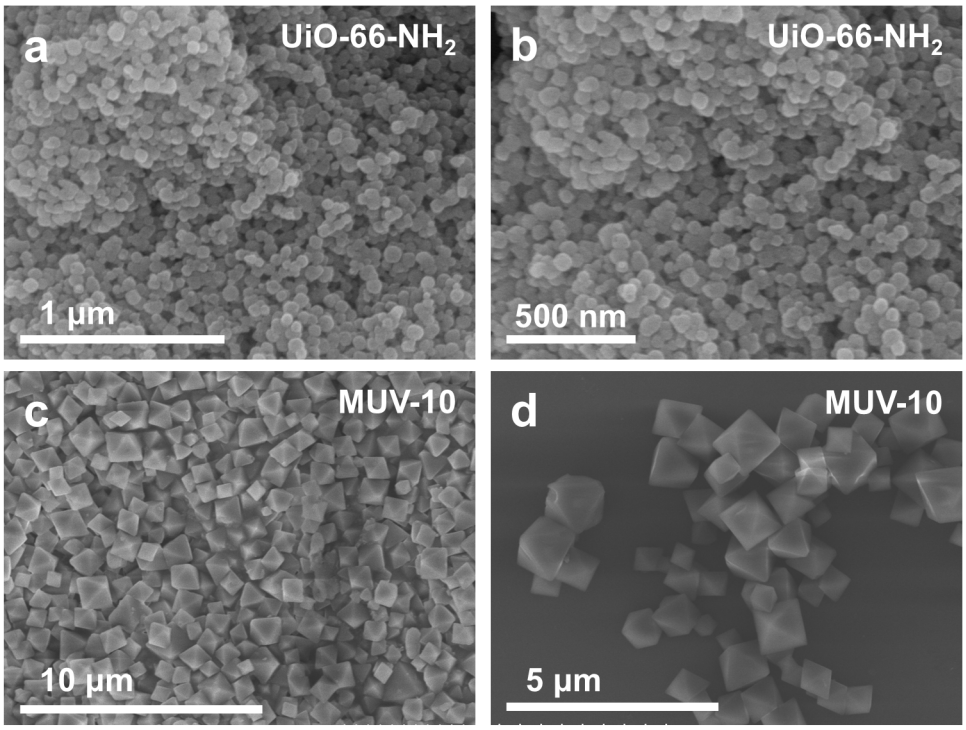

Fig. S3 SEM images of (a-b) UiO-66-NH_2 and (c-d) MUV-10.

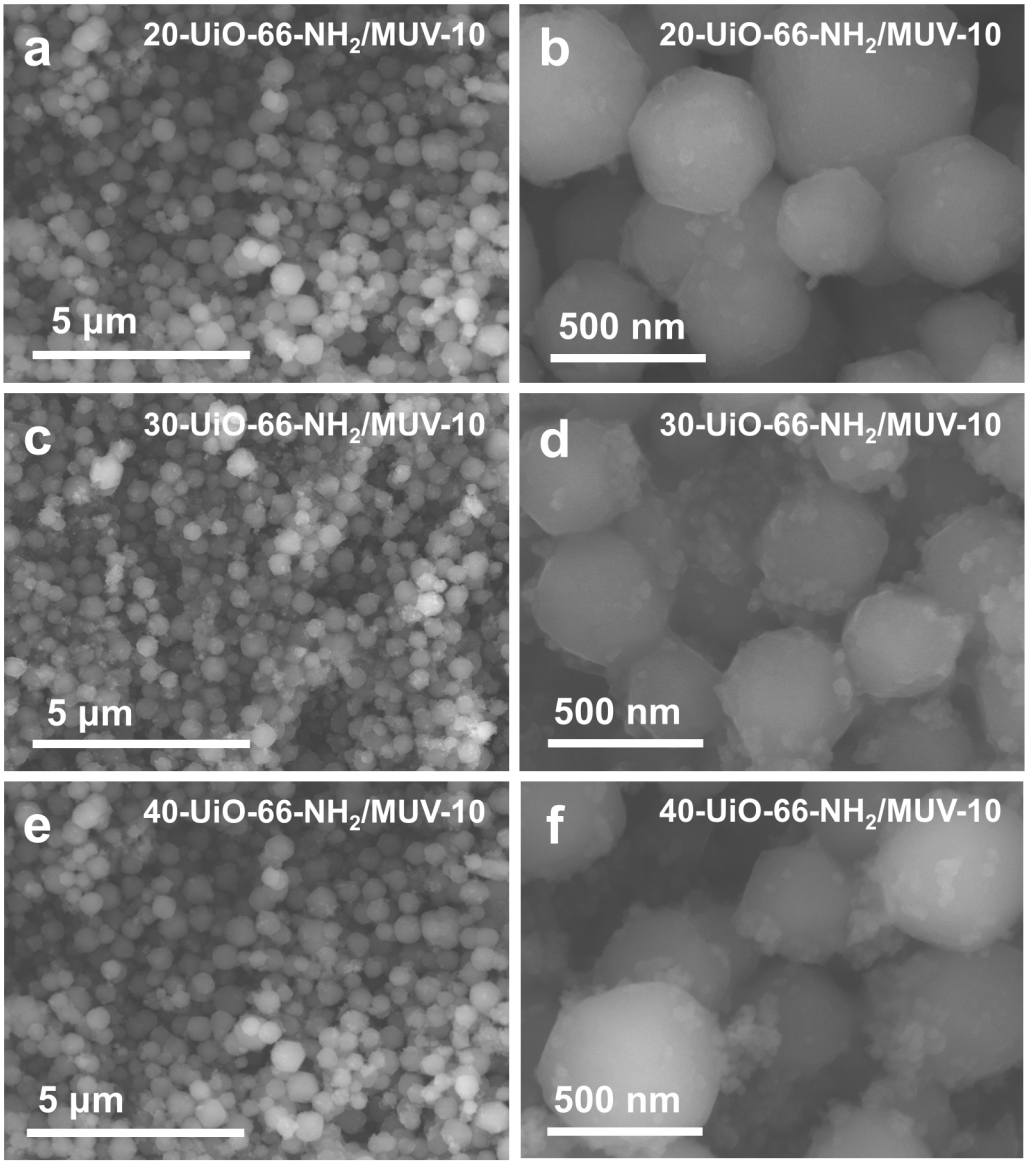

Fig. S4 SEM images of (a-b) 20-UiO-66-NH_2/MUV-10, (c-d) 30-UiO-66-NH_2/MUV-10, and (e-f) 40-UiO-66-NH_2/MUV-10.

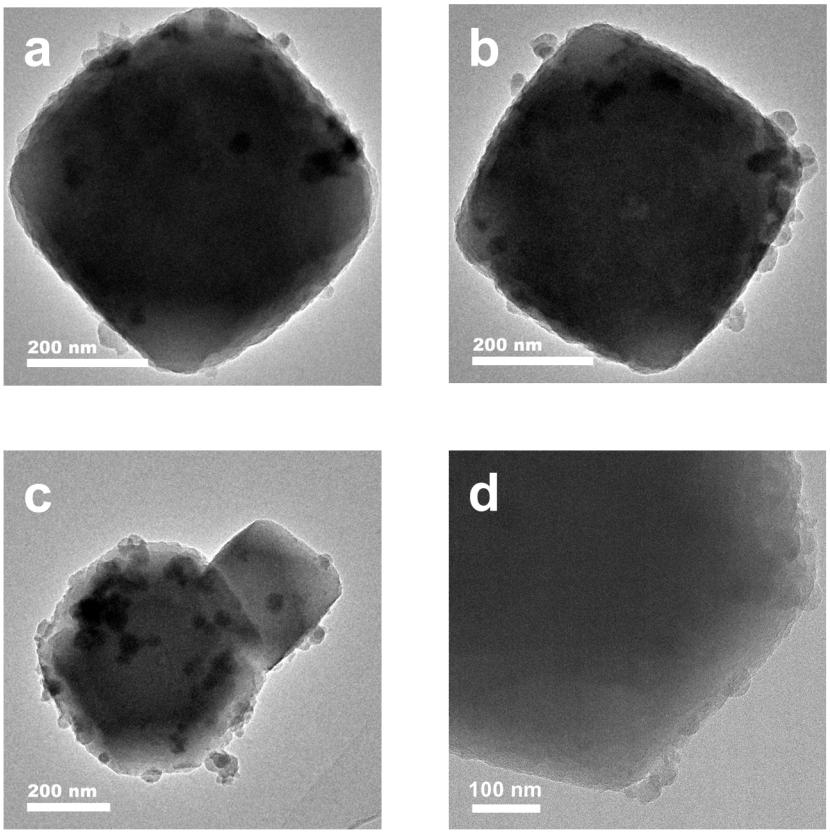

Fig. S5 (a-d) STEM images of UiO-66-NH_2/MUV-10.

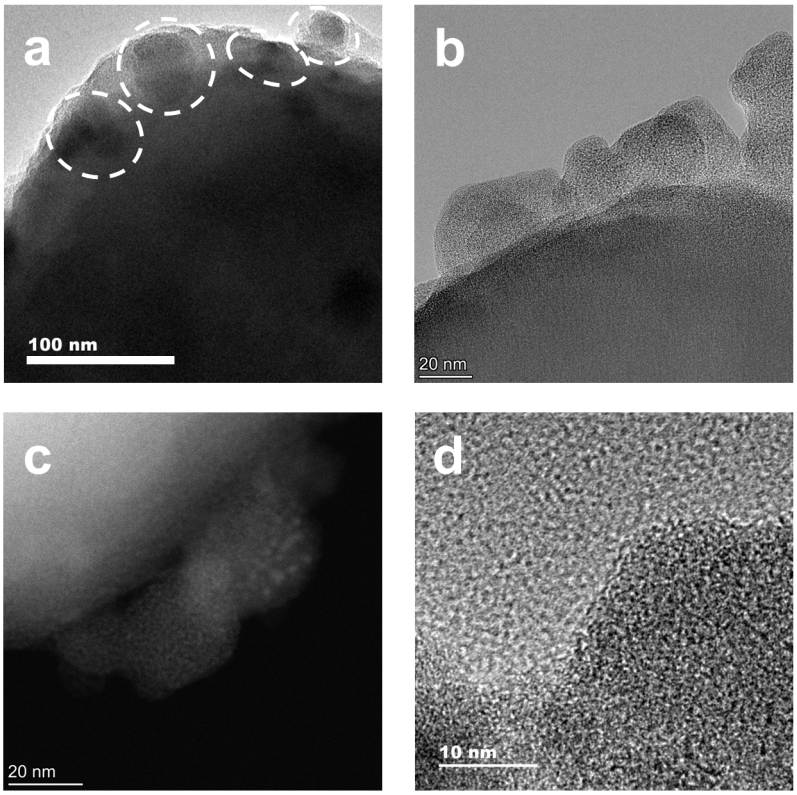

Fig. S6 (a-d) High-resolution HAADF-STEM images of UiO-66-NH_2/MUV-10.

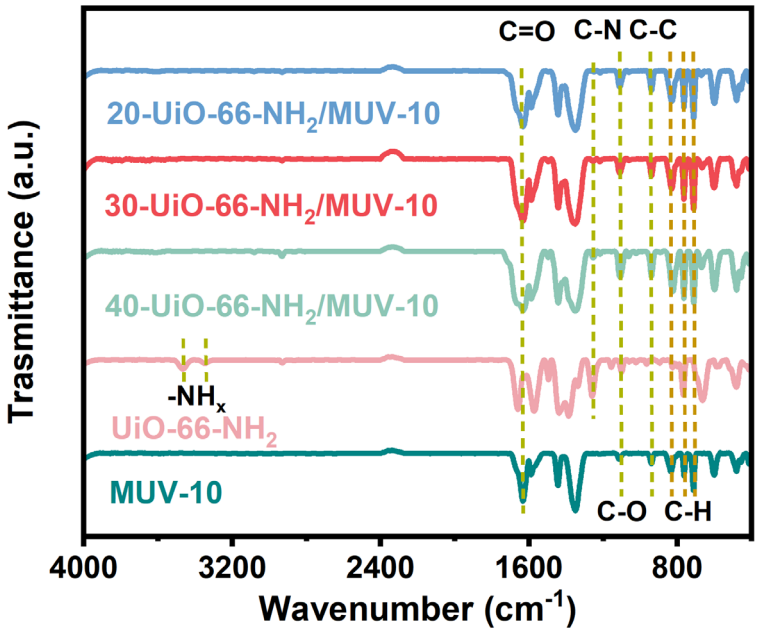

Fig. S7 FT-IR spectra of UiO-66-NH_2, MUV-10, 20-UiO-66-NH_2/MUV-10, 30-UiO-66-NH_2/MUV-10, and 40-UiO-66-NH_2/MUV-10.

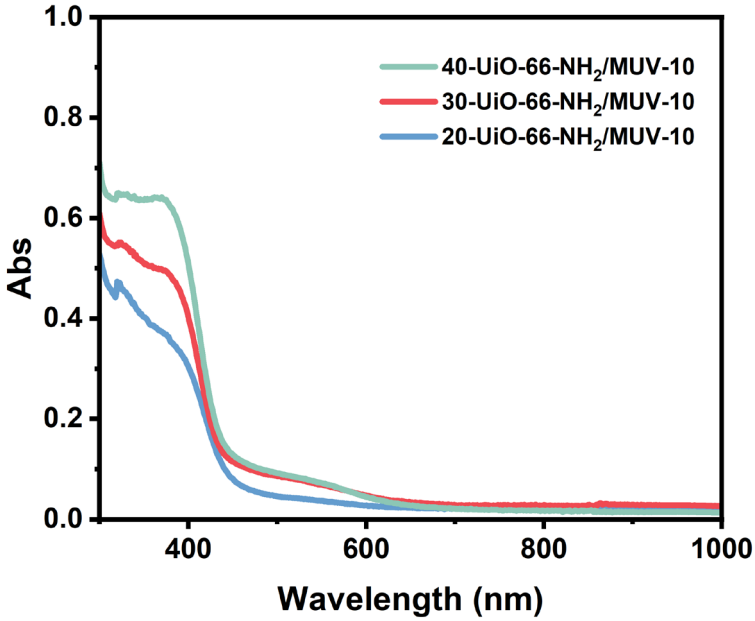

Fig. S8 UV-vis absorption spectra of 20-UiO-66-NH_2/MUV-10, 30-UiO-66-NH_2/MUV-10, and 40-UiO-66-NH_2/MUV-10.

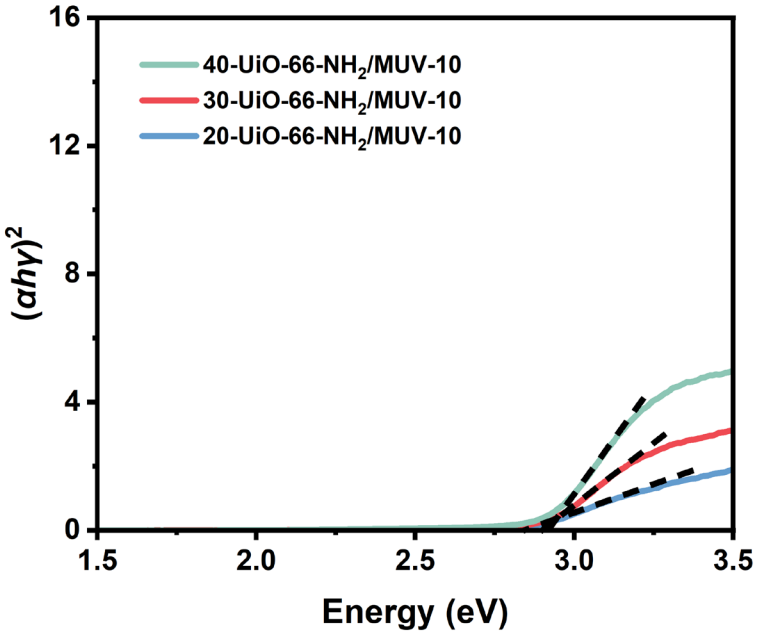

Fig. S9 Plots of $(\alpha h\gamma)^2$ against the photonic energy of 20-UiO-66-NH_2/MUV-10, 30-UiO-66-NH_2/MUV-10, and 40-UiO-66-NH_2/MUV-10.

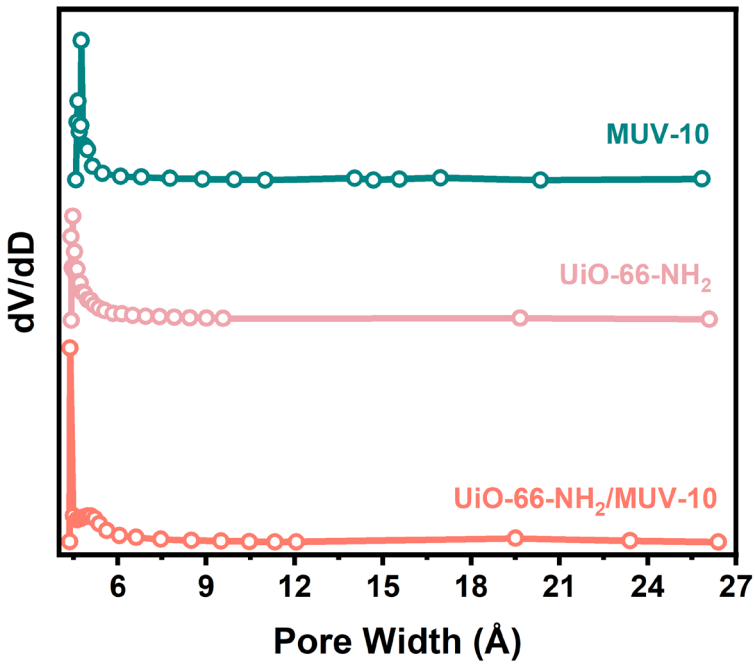

Fig. S10 Corresponding PSD of N_2 adsorption-desorption isotherms at 77 K for UiO-66-NH_2, MUV-10, and UiO-66-NH_2/MUV-10.

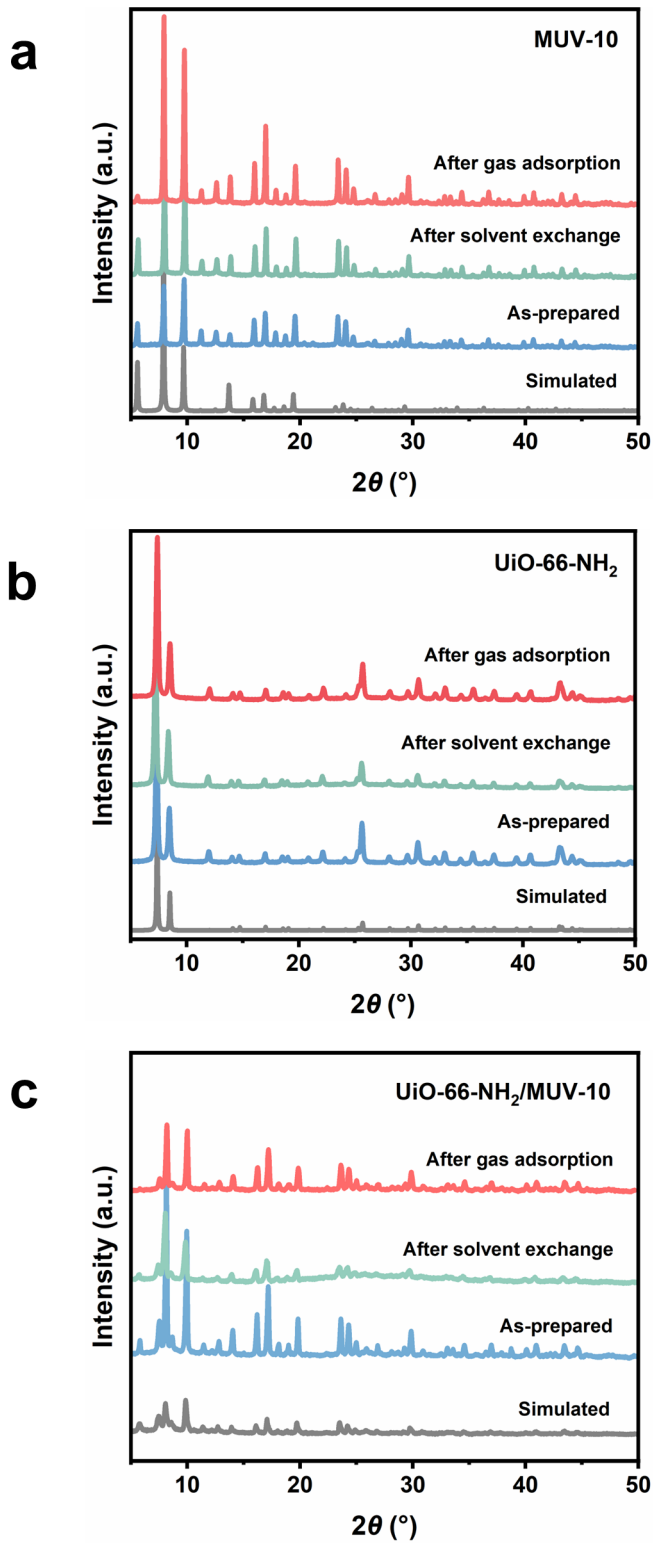

Fig. S11 PXRD patterns of (a) MUV-10, (b) UiO-66-NH_2, and (c) UiO-66-NH_2/MUV-10.

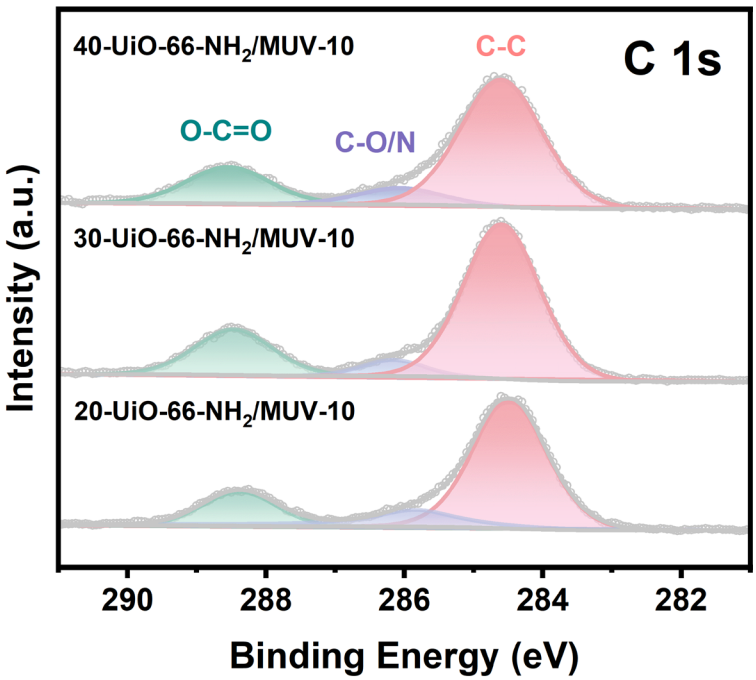

Fig. S12 XPS spectra of C 1s in 20-UiO-66-NH_2/MUV-10, 30-UiO-66-NH_2/MUV-10, and 40-UiO-66-NH_2/MUV-10.

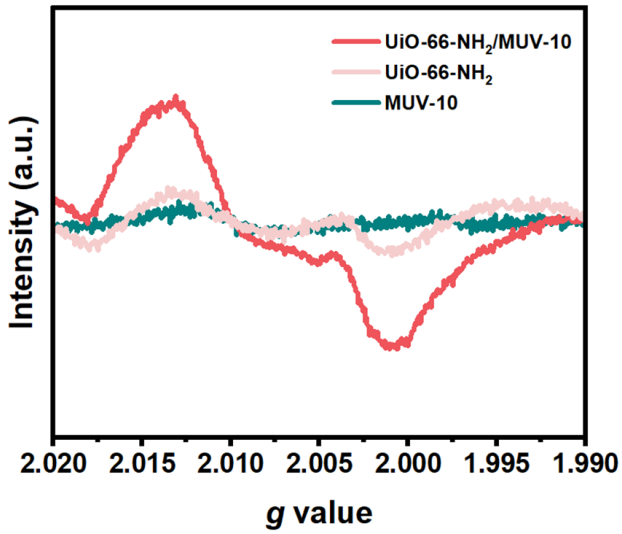

Fig. S13 The ESR spectrum of UiO-66-NH_2, MUV-10 and UiO-66-NH_2/MUV-10.

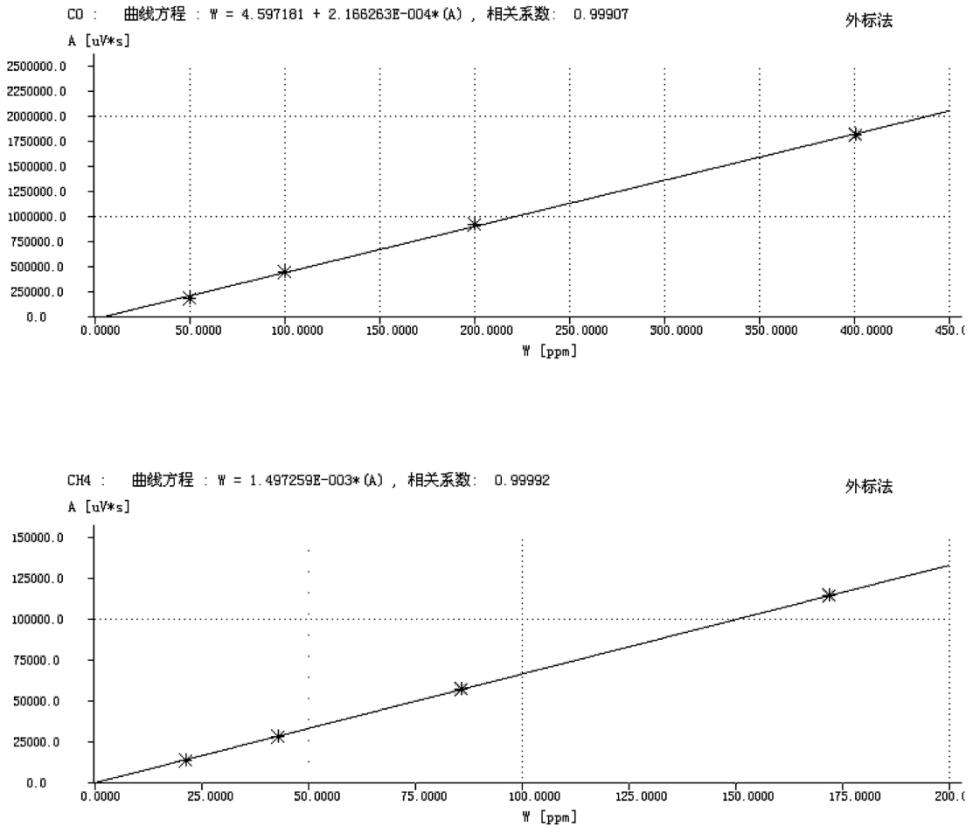

Fig. S14 Characterization of products by gas chromatography (GC).

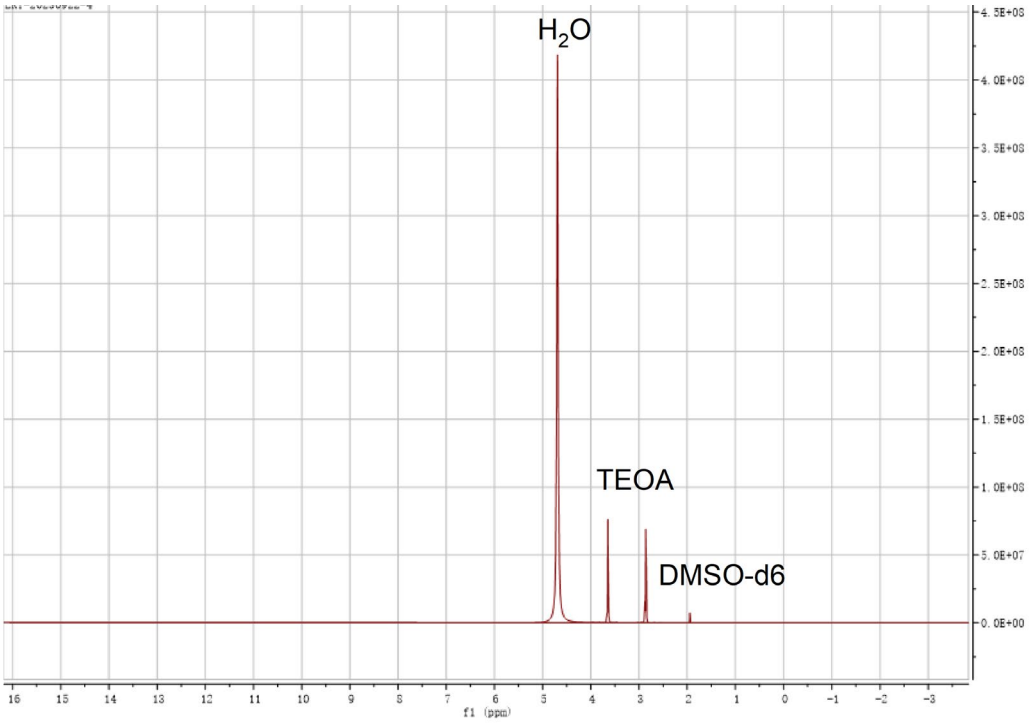

Fig. S15 Nuclear magnetic analysis of UiO-66-NH_2/MUV-10 photoreduction CO_2 products (in DMSO-d6).

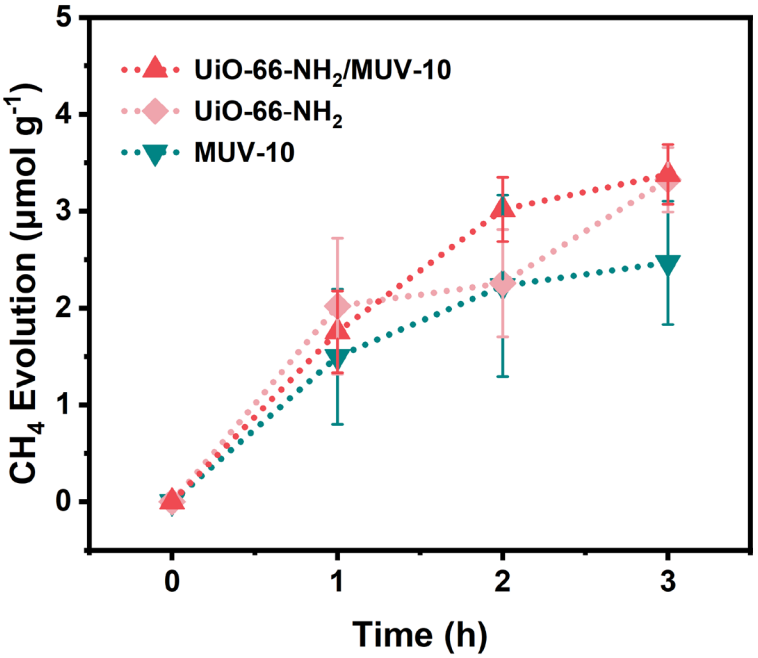

Fig. S16 Photocatalytic CH_4 evolution over time for MUV-10, UiO-66-NH_2, and UiO-66-NH_2/MUV-10 with $\lambda > 400$ nm filter.

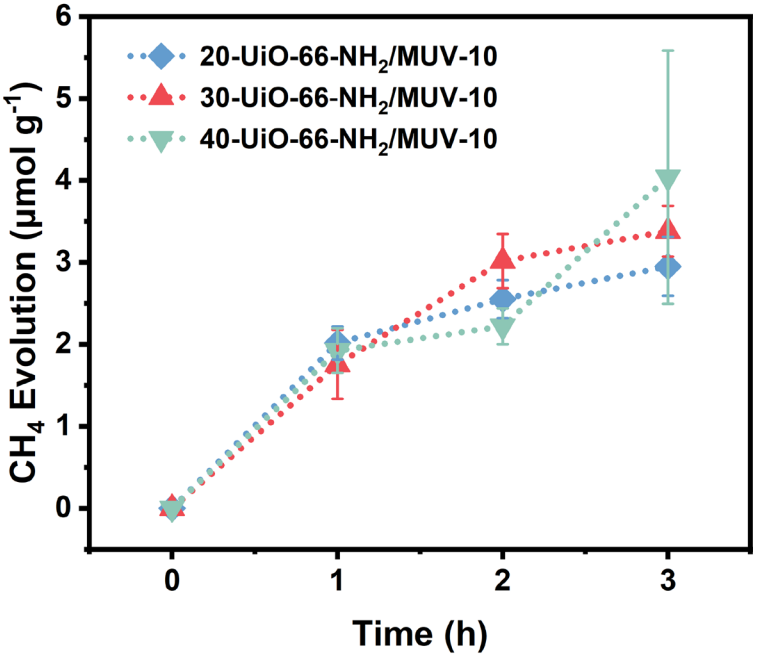

Fig. S17 Photocatalytic CH_4 evolution over time for 20-UiO-66-NH_2/MUV-10, 30-UiO-66-NH_2/MUV-10, and 40-UiO-66-NH_2/MUV-10 with $\lambda > 400$ nm filter.

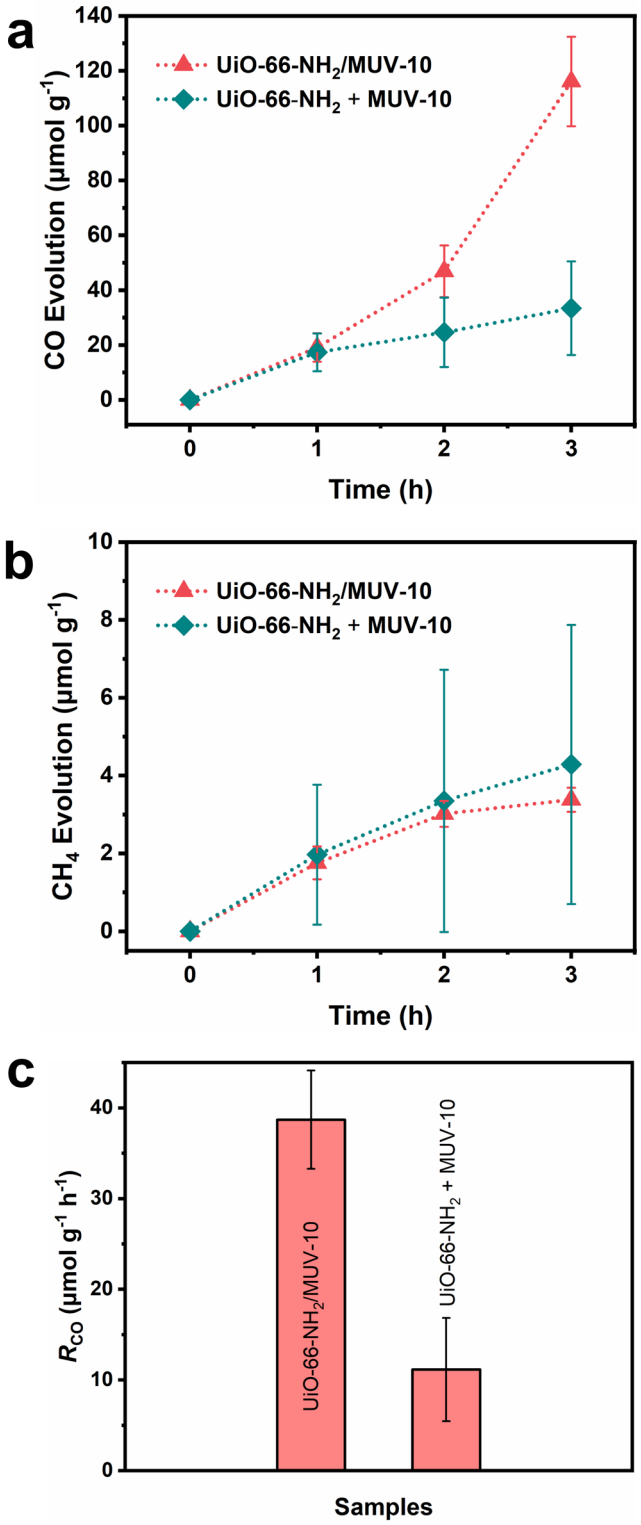

Fig. S18 (a) Photocatalytic CO evolution over time for mechanical mixture (UiO-66-NH_2 + MUV-10) and UiO-66-NH_2/MUV-10 with λ > 400 nm filter. (b) Photocatalytic CO evolution over time for mechanical mixture (UiO-66-NH_2 + MUV-10) and UiO-66-NH_2/MUV-10 with λ>400 nm filter. (c) Mass-normalized CO_2RR rates of mechanical mixture (UiO-66-NH_2 + MUV-10) and UiO-66-NH_2/MUV-10 with λ>400 nm filter.

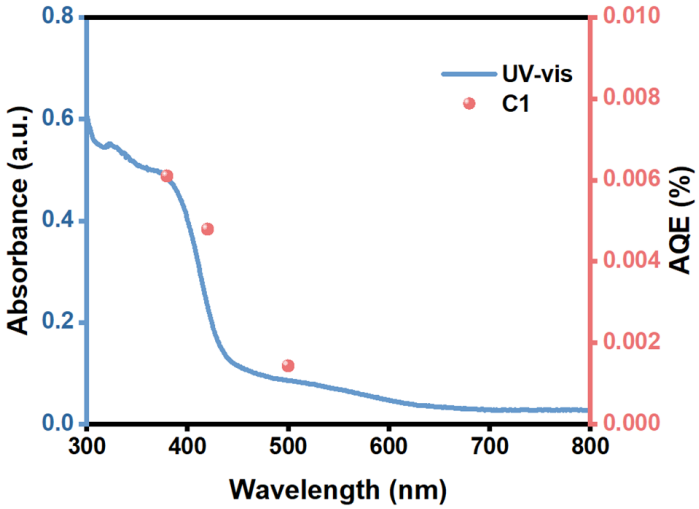

Fig. S19 Wavelength-dependent AQE for the 30-UiO-66-NH_2/MUV-10 photocatalyst.

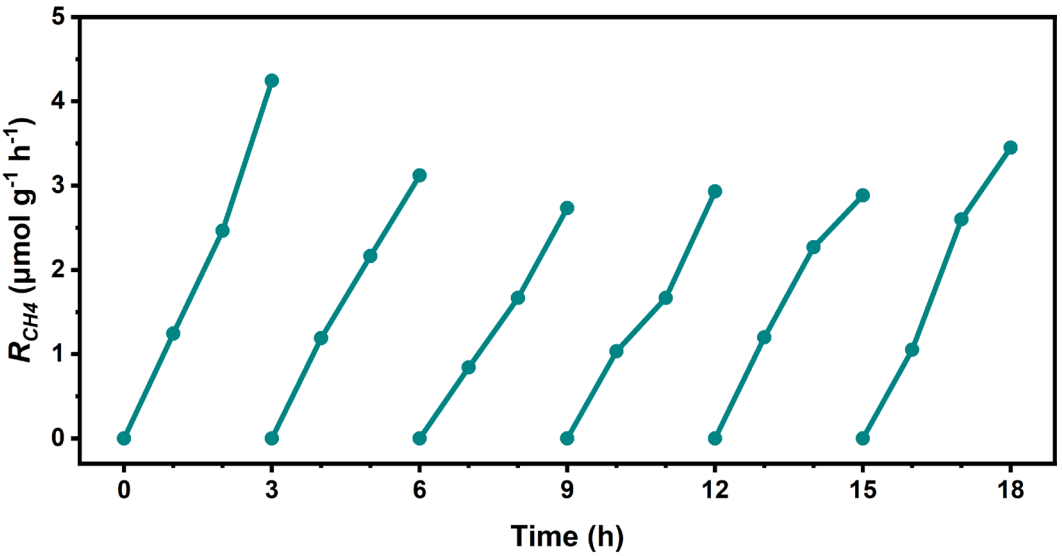

Fig. S20 Cyclic stability for CH_4 evolution of UiO-66-NH_2/MUV-10.

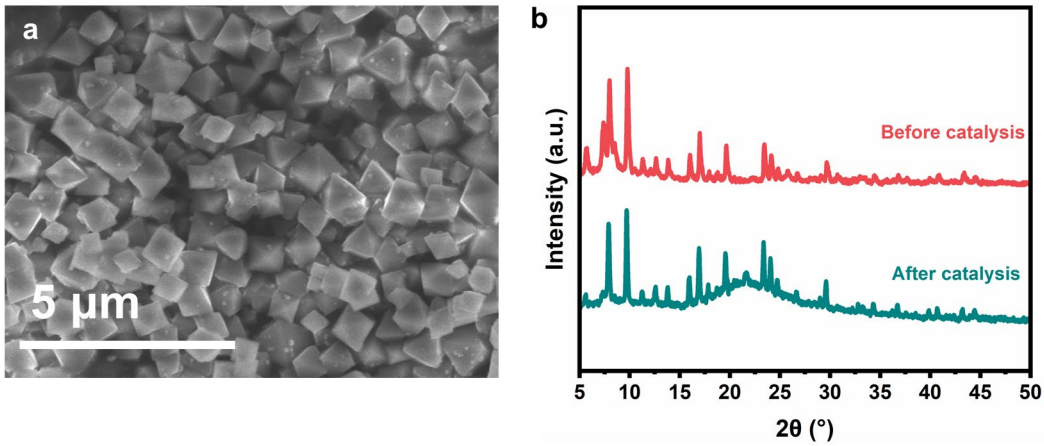

Fig. S21 Stability of UiO-66-NH_2/MUV-10. (a) SEM image of UiO-66-NH_2/MUV-10 after photocatalysis. (b) PXRD patterns of UiO-66-NH_2/MUV-10 before and after photocatalysis.

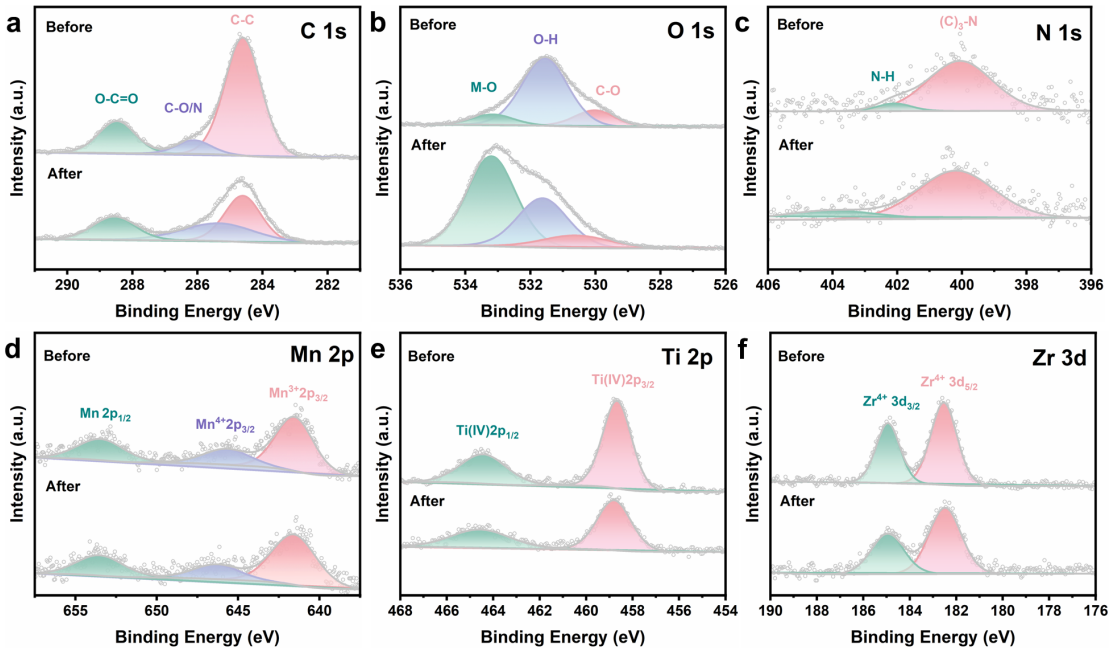

Fig. S22 Stability of UiO-66-NH_2/MUV-10. XPS spectrum (a) C 1s, (b) O 1s, (c) N 1s, (d) Zr 3d, (e) Mn 2p and (f) Ti 2p in UiO-66-NH_2/MUV-10 before and after photocatalysis.

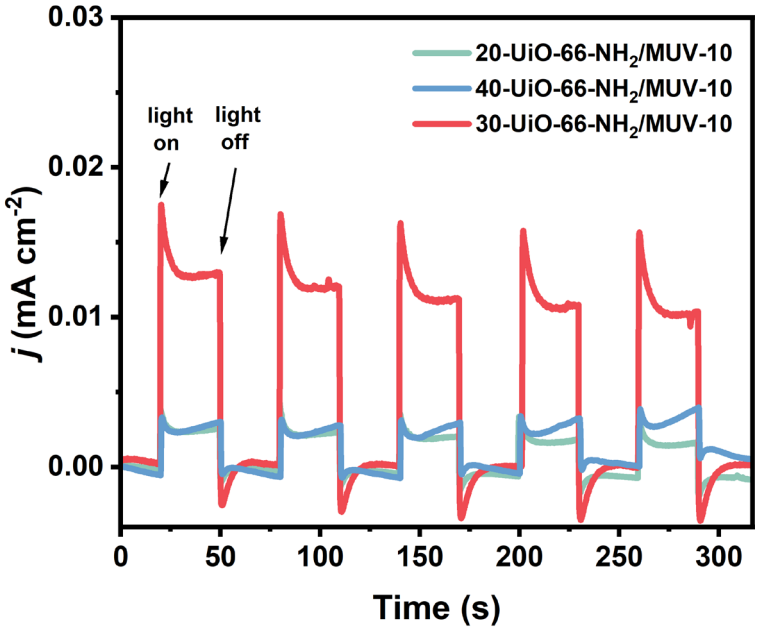

Fig. S23 Transient photocurrent density of 20-UiO-66-NH_2 /MUV-10, 30-UiO-66-NH_2 /MUV-10, and 40-UiO-66-NH_2 /MUV-10.

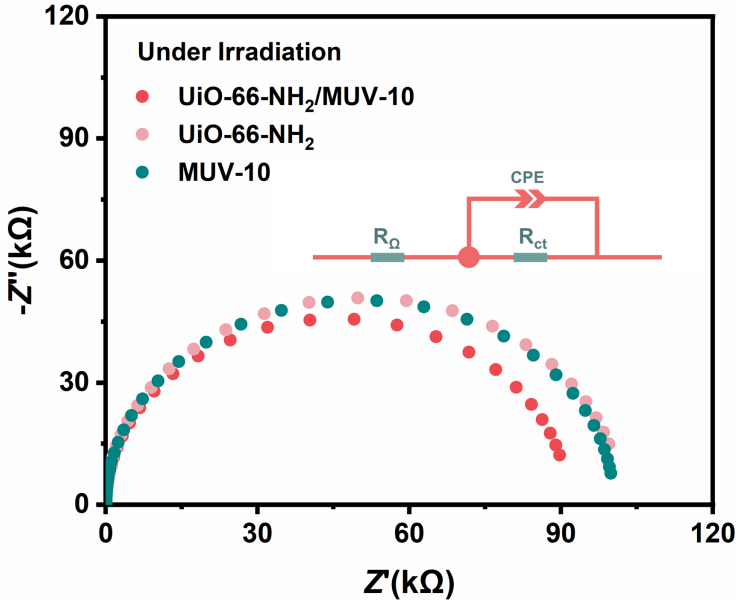

Fig. S24 AC impedance of MUV-10, UiO-66-NH_2, and UiO-66-NH_2/MUV-10 under light irradiation.

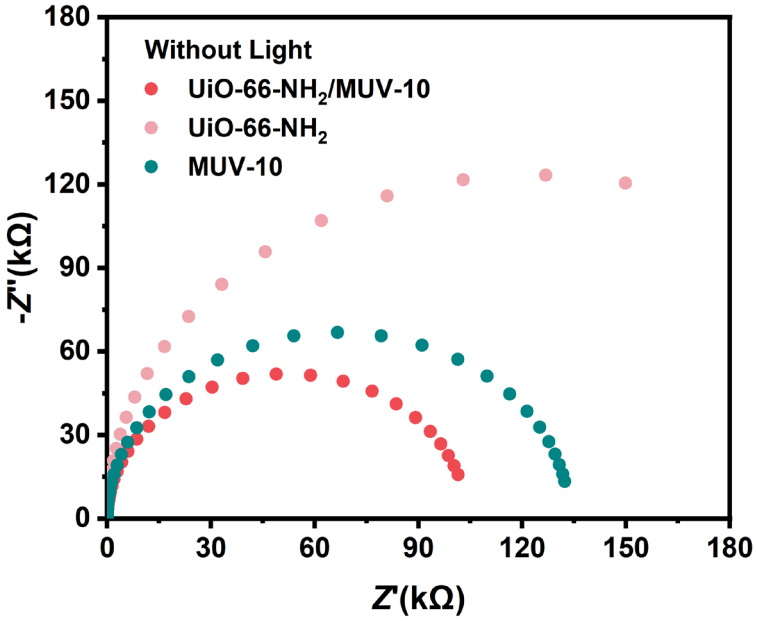

Fig. S25 AC impedance of MUV-10, UiO-66-NH_2, and UiO-66-NH_2/MUV-10 without light irradiation.

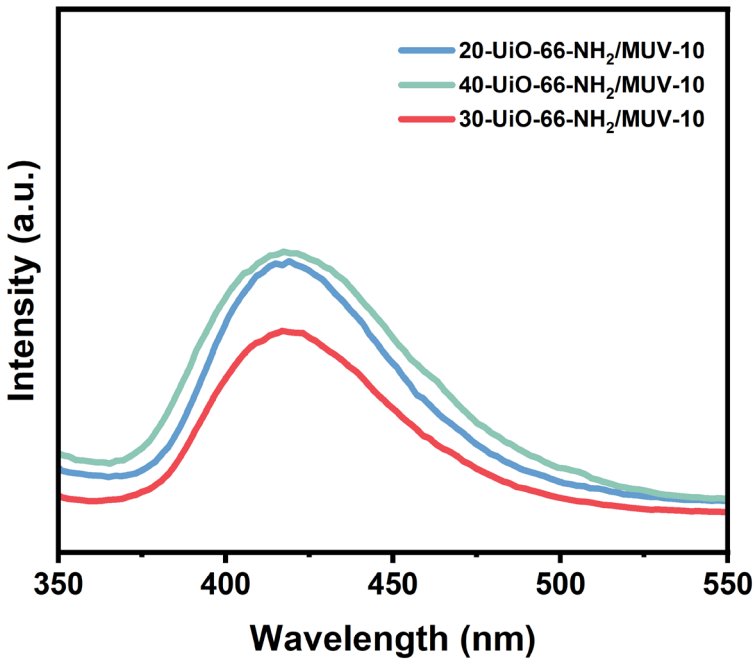

Fig. S26 PL spectra of 20-UiO-66-NH_2/MUV-10, 30-UiO-66-NH_2/MUV-10, and 40-UiO-66-NH_2/MUV-10.

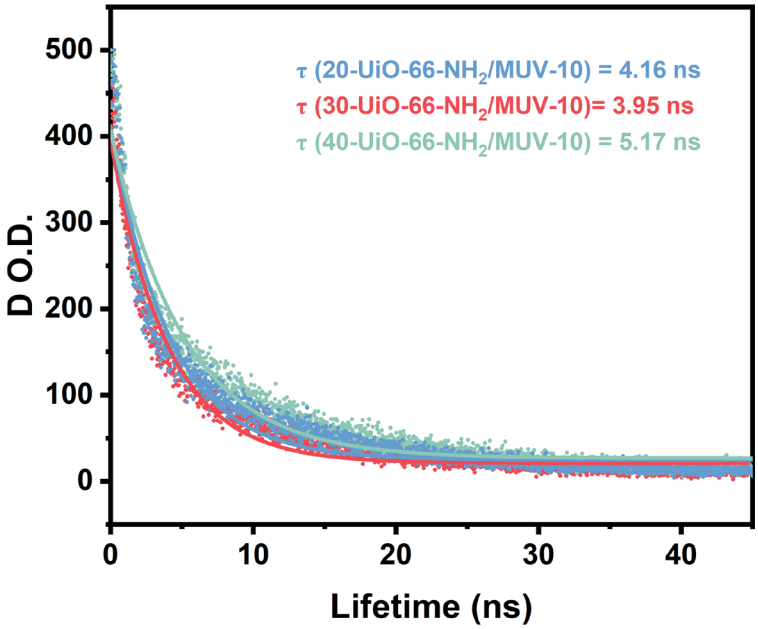

Fig. S27 TRPL spectra of 20-UiO-66-NH_2 /MUV-10, 30-UiO-66-NH_2 /MUV-10, and 40-UiO-66-NH_2 /MUV-10.

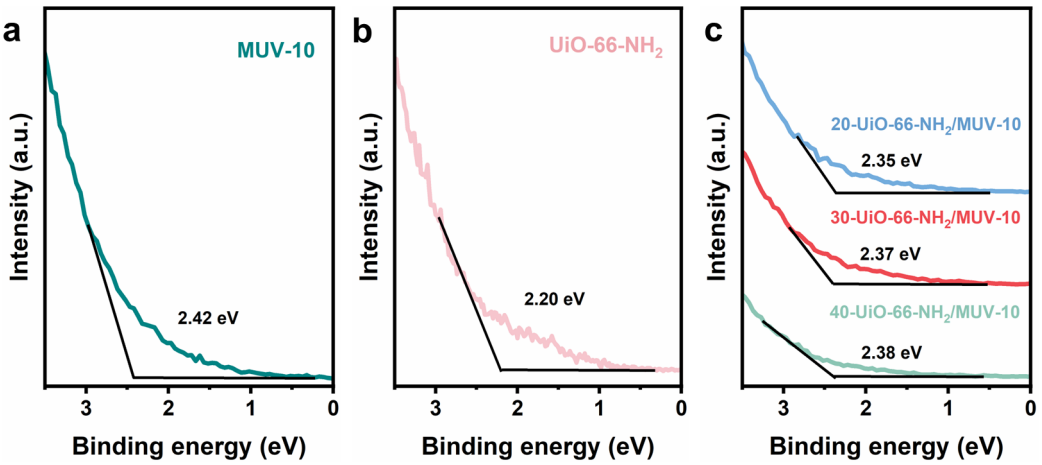

Fig. S28 Valence band XPS of (a) MUV-10, (b) UiO-66-NH_2 and (c) 20-UiO-66-NH_2/MUV-10, 30-UiO-66-NH_2/MUV-10, and 40-UiO-66-NH_2/MUV-10.

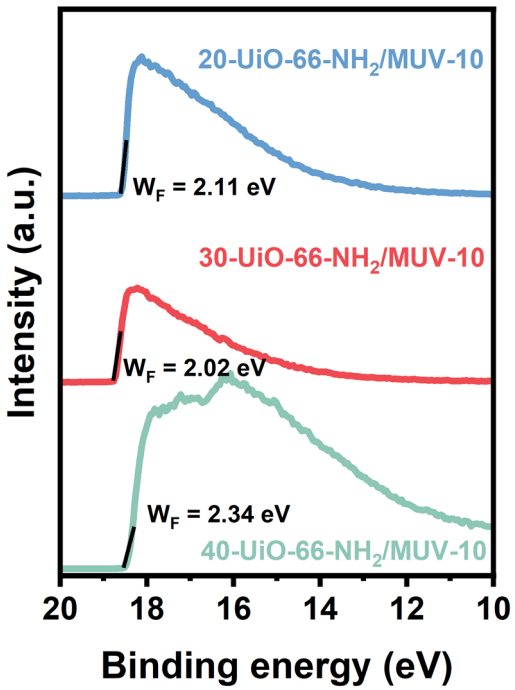

Fig. S29 UPS spectra of 20-UiO-66-NH_2/MUV-10, 30-UiO-66-NH_2/MUV-10, and 40-UiO-66-NH_2/MUV-10.

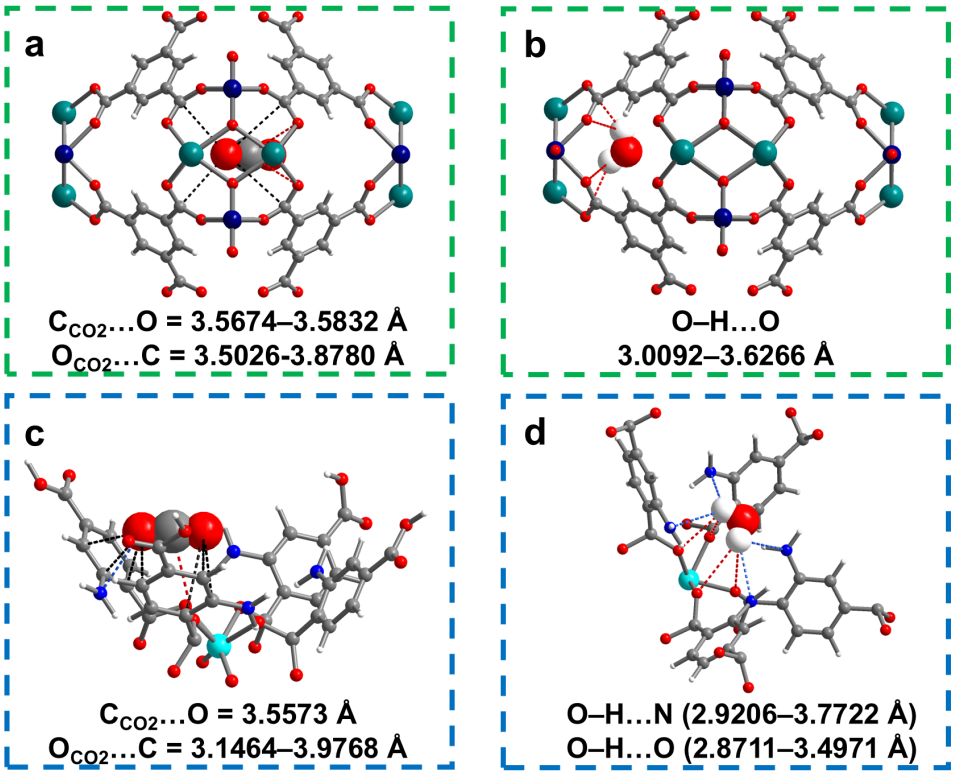

Fig. S30 (a) CO_2 and (b) H_2O binding sites in MUV-10, (c) CO_2 and (d) H_2O binding sites in UiO-66-NH_2 absorbents determined by GCMC simulation.

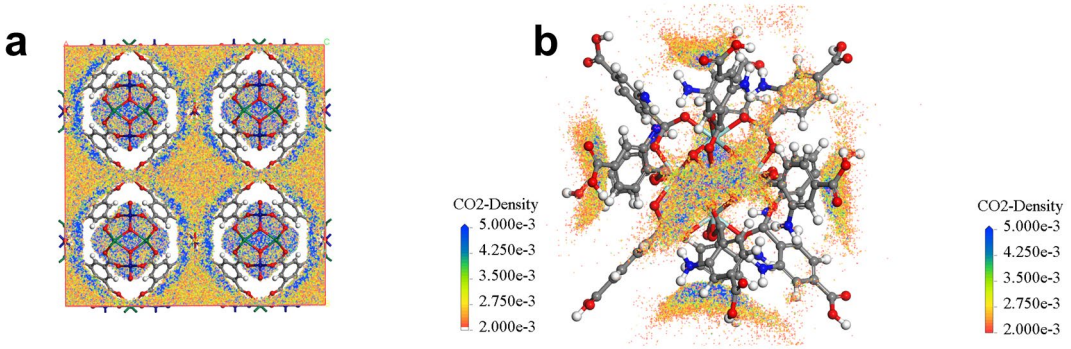

Fig. S31 GCMC simulation for density distributions of CO_2 at 298 K for (a) MUV-10 and (b) UiO-66-NH_2.

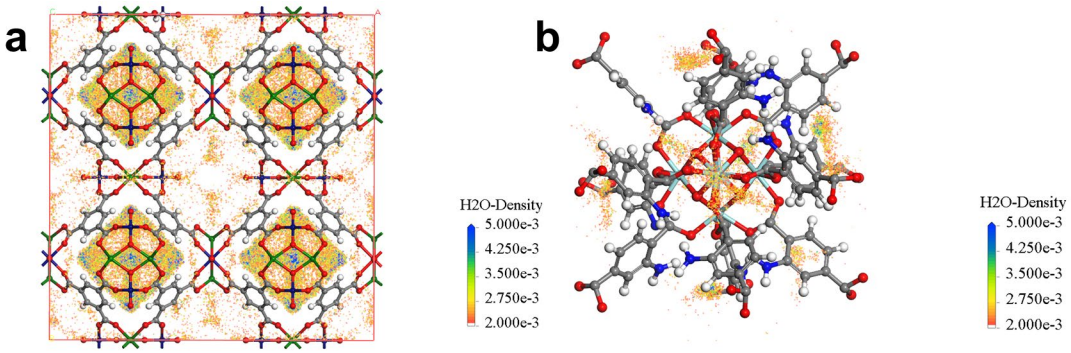

Fig. S32 GCMC simulation for density distributions of H_2O at 298 K for (a) MUV-10 and (b) UiO-66-NH_2.

Table S1. Calculation details about the AQE of UiO-66-NH_2/MUV-10.

I×S (W)	λ (nm)	A	v_{CO} (mol s^{-1})	v_{CH4} (mol s^{-1})	AQE (%)
0.292	380	0.48	7.98637×10^{-12}	1.41738×10^{-12}	0.006
0.229	420	0.23	3.20112×10^{-12}	3.08333×10^{-12}	0.005
0.512	500	0.086	1.2375×10^{-12}	1.79688×10^{-12}	0.001

Table S2. Summary of the photocatalytic activity with the recently reported photocatalysts in direct gas–solid-phase photocatalytic conversion of CO_2.

Photocatalysts	Conditions	Light intensity (W)	Main products (μmol g^{-1} h^{-1})	AQE(%)	Ref.
UiO-66-NH_2/MUV-10	CO_2, H_2O, $\lambda > 400$ nm	300	CO: 37.7	0.005 (420 nm)	This work
PCN-601	CO_2, H_2O, $\lambda > 410$ nm	/	CH_4: 10.1; CO: 6.0	/	S1
2D porphyrin-based Mn-MOF	CO_2, H_2O, simulated solar irradiation (AM 1.5G)	300	CH_4: 53; CO: 21	/	S2
$CsPbBr_3$@ZIF-67	CO_2, H_2O, A 100 W Xe lamp with AM 1.5G filter	100	CH_4: 2.35; CO: 0.49	0.035 (386 nm)	S3
CPO-27-Mg/TiO_2	CO_2, H_2O, $\lambda = 365$ nm	4	CO: 4.09; CH_4: 2.35; O_2: 6.29	/	S4
$CsPbBr_3$ QDs/UiO-66(NH_2)	CO_2, H_2O, $\lambda > 420$ nm	300	CH_4: 0.26; CO: 8.21	/	S5
HKUST-1/TiO_2	CO_2, H_2O, 450 W Xe lamp with an AM 1.5G filter	450	CO: 256.35	/	S6
HCP-3	CO_2, H_2O, $\lambda > 325$ nm	300	CH_4: 0.3; CO: 5.1	0.0005 (400 -900 nm)	S7
HCP-TiO_2-FG	CO_2, H_2O, $\lambda > 420$ nm	300	CH_4: 27.62	/	S8
Cu/TiO_2-AG	0.5 vol% O_2 in CO_2 UV-/vis light (320–500 nm)	2.5	CO: 28.2	/	S9
VO-$STMn_{0.2}$	CO_2, H_2O	300	CH_4: 6.07	0.35 (380 nm)	S10
Co-MOF/Cu_2O	CO_2, H_2O, 300 W Xe lamp with a 420 nm cut-off optical filter	300	CO: 3.83	/	S11
CCN	CO_2, H_2O, $\lambda > 400$nm	300	CO: 25.7	0.33 (420 nm)	S12
$CsPbBr_3$/Au/TiO_2	CO_2, AM 1.5 G, 100 mW·cm^{-2}	300	CO: 17.27 CH_4: 1.22	/	S13

Table S3. Fitting results of R_{Ω} and R_{ct} of the EIS Nyquist plots.

Sample	R_{Ω}/Ω (without light)	R_{Ω}/Ω (light)	R_{ct}/kΩ (without light)	R_{ct}/kΩ (light)	*C*p (without light)	*C*p (light)
MUV-10	54.37	53.93	133.6	100.4	1.196×10^{-5}	1.225×10^{-5}
UiO-66-NH_2	36.72	50.2	246.6	101.6	5.186×10^{-5}	2.348×10^{-5}
UiO-66-NH_2/MUV-10	56.74	49.69	103.9	91.36	2.389×10^{-5}	2.375×10^{-5}

References

S1. Z.B. Fang, T.T. Liu, J. Liu, S. Jin, X.P. Wu, X.Q. Gong, K. Wang, Q. Yin, T.F. Liu, R. Cao, H.C. Zhou, *J. Am. Chem. Soc.,* 2020, **142**, 12515–12523.

S2. J.-H. Qin, P. Xu, Y.-D. Huang, L.-Y. Xiao, W. Lu, X.-G. Yang, L.-F. Ma, S.-Q. Zang, *Chem. Commun*., 2021, **57**, 8468.

S3. Z.-C. Kong, J.-F. Liao, Y.-J. Dong, Y.-F. Xu, H.-Y. Chen, D.-B. Kuang, C.-Y. Su, *ACS Energy Lett*., 2018, **3**, 2656–2662.

S4. M. Wang, D. Wang, Z. Li, *Appl. Catal. B-Environ*., 2016, **183**, 47–52.

S5. S. Wan, M. Ou, Q. Zhong, X. Wang, *Chem. Eng. J*., 2019, **358**, 1287–1295.

S6. X. He, Z. Gan, S. Fisenko, D. Wang, H.M. El-Kaderi, W.N. Wang, *ACS Appl. Mater. Interfaces*, 2017, **9**, 9688–9698.

S7. G.E.M. Schukraft, R.T. Woodward, S. Kumar, M. Sachs, S. Eslava, C. Petit, *ChemSusChem*, 2021, **14**, 1720–1727.

S8. S. Wang, M. Xu, T. Peng, C. Zhang, T. Li, I. Hussain, J. Wang, B. Tan, *Nat. Commun*., 2019, **10**, 676.

S9. S. Kreft, R. Schoch, J. Schneidewind, J. Rabeah, E.V. Kondratenko, V. A. Kondratenko, H. Junge, M. Bauer, S. Wohlrab, M. Beller, *Chem*, 2019, **5**, 1818–1833.

S10. Y. Gao, M. Zhang, Y. Jin, M. Zhou, Y. Mao, J. Sun, W. Wang, Z. Song, *Appl. Catal. B.,* 2023, **341**, 123348.

S11. D. Wen-Wen, J. Jing, W. Ye, A. Jun-Rong, Y. Ou-Yang, G. Xue-Jing, L. Yun-Ling, Z. Jun, L. Dong-Sheng, *Chem. Eng. J.,* 2022, **438**, 135622.

S12. Y. Li, Y. Xue, X. Gao, L. Wang, X. Liu, Z. Wang, S. Shen, *Adv. Funct. Mater.,* 2023, **34**, 2312634.

S13. W. Song, K. C. Chong, G. Qi, Y. Xiao, G. Chen, B. Li, Y. Tang, X. Zhang, Y. Yao, Z. Lin, Z. Zou, B. Liu, *J. Am. Chem. Soc.,* 2024, **146**, 3303–3314.